Chinese Chemical Letters 36 (2025) 109936

Contents lists available at ScienceDirect

Chinese Chemical Letters

journal homepage: www.elsevier.com/locate/cclet

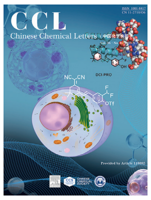

Design and fabrication of Cu^{I}/Cu^{II}-MOF-incorporated hydrogel photocatalysts for synergy removal of Cr(VI) and congo red

Quanquan Li[a,b,1], Chenzhu Zhao[a,1], Shanshan Jia[a], Qiang Chen[a], Xusheng Li[a], Mengyao She[a,c], Hua Liu[a,d,*], Ping Liu[a,*], Yaoyu Wang[a], Jianli Li[a,*]

[a] College of Chemistry & Materials Science, Northwest University, Xi'an 710127, China
[b] College of New Energy, Yulin University, Yulin 719000, China
[c] College of Life Sciences, Northwest University, Xi'an 710069, China
[d] College of Chemical Engineering and Technology, Taiyuan University of Science and Technology, Taiyuan 030024, China

ARTICLE INFO

Article history:
Received 9 March 2024
Revised 9 April 2024
Accepted 28 April 2024
Available online 29 April 2024

Keywords:
Metal-organic framework
Hydrogel photocatalyst
Heterogeneous photocatalyst
Synergy removal effect
Cr(VI) and congo red removal

ABSTRACT

Metal-organic frameworks (MOFs) provide great prospective in the photodegradation of pollutants. Nevertheless, the poor separation and recovery hamper their pilot- or industrial-scare applications because of their microcrystalline features. Herein, this challenge can be tackled by integrating Cu-MOFs into an alginate substrate to offer environmentally friendly, sustainable, facile separation, and high-performance MOF-based hydrogel photocatalysis platforms. The Cu^{II}-MOF **1** and Cu^{I}-MOF **2** were initially synthesized through a direct diffusion and single-crystal to single-crystal (SCSC) transformation method, respectively, and after the immobilization into alginate, more effective pollutant decontamination was achieved *via* the synergistic effect of the adsorption feature of hydrogel and *in situ* photodegradation of Cu-MOFs. Specifically, Cu-MOF-alginate composites present an improved and nearly completed Cr(VI) elimination at a short time of 15–25 min. Additionally, the congo red (CR) decolorization can be effectively enhanced in the presence of Cr(VI), and **1**-alginate showed superior simultaneous decontamination efficiency of CR and Cr(VI) with 99% and 78%, respectively. Furthermore, Cu-MOF-alginate composites can maintain a high pollutant removal after over 10 continuous cycles (95% for Cr(VI) after 14 runs, and 90% for CR after 10 runs). Moreover, the Cr(VI)/CR degradation mechanism for Cu-MOF-alginate composite was investigated.

Water contamination is an urgent environmental issue because of rapid industrialization [1–4]. Especially, industrial wastewater commonly contains large amounts of organics and heavy metals, which pose a serious threat to health and water security [5–7]. Photocatalysis, as a clean, green, and sustainable technology, has been harnessed to address the challenges concerning water contamination [8–11]. To date, large amounts of photocatalysts have been designed and developed to remove organic compounds or heavy metal pollutants [12–15]. Nonetheless, only a limited number of photocatalysts have been prepared and reported on the simultaneous elimination of metals and organics [16–19]. Additionally, to supply the demands of sunlight utilization, band structure, or carrier separation, most photocatalysts were fabricated in small-sized forms and hard to isolate and recover, resulting in second pollution and poor recycling [20]. Accordingly, to overcome these drawbacks, developing multiple-effect photocatalysts, as well as structuring MOFs into special shapes with a higher number of dimensions are very urgent and meaningful.

Hydrogels have been recognized as a promising platform to support photocatalysts and acquire effective energy conversion, due to the features of high surface areas, splendid adsorption capacities, good flexibility, high ionic conductivity, and environmental compatibility [9,20,21]. The integration of hydrogel with many traditional inorganic semiconductors including typical TiO_2 has been developed to fabricate inorganic semiconductor-based hydrogel photocatalysts for water management [22–24]. However, traditional inorganic semiconductor materials commonly suffer from wide bandgap, low quantum efficiency, worse light adsorption, or rapid carrier recombination [20]. Tremendous efforts need to be devoted to developing alternatives. Metal-organic frameworks (MOFs) are appearing as prospective alternatives with excellent photocatalysis towards the potential simultaneous elimination of metals and organics, owing to the well-fined and customized structure/cavity at the atom level, as well as the designability and tunability of band structure and photoadsorption [25–32]. Therefore,

---

* Corresponding authors.
E-mail addresses: lh128307@163.com (H. Liu), liuping@nwu.edu.cn (P. Liu), lijianli@nwu.edu.cn (J. Li).

[1] These authors contributed equally to this work.

https://doi.org/10.1016/j.cclet.2024.109936

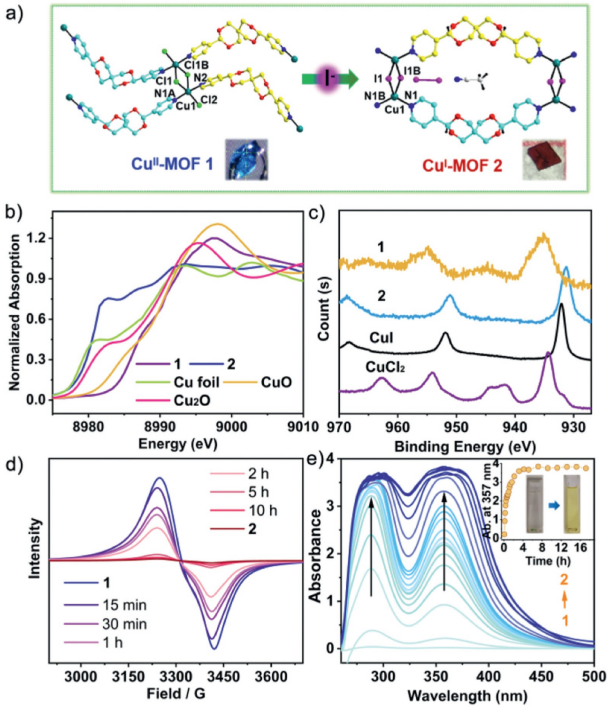

Fig. 1. (a) A structural view of the single-crystal to single-crystal (SCSC) transformation, and the metal coordination environment of **1** and **2**. The symmetry codes: for **1**, *A* = *x*-1, -*y* + 1/2, *z* + 1/2; B = -*x*, -*y* + 1, -*z* + 1; for **2**, *A* = -*x*, -*y* + 1, -*z*; *B* = -*x*, *y*, -*z*. (b) The XANES spectra and (c) Cu 2p high-resolution XPS survey of **1** and **2**. (d) EPR spectra of the reduction process (X band, 9.83 GHz, room temperature). (e) Time-dependent transformation process by detecting I_3^- of **1** in the NaI acetonitrile/water solution.

a strategy of integrating hydrogel and MOF may accelerate more environmental and efficient water remediation. Herein, we present a general structuring way through the combination of Cu-MOF and hydrogel to offer visible-light induced Cu-MOF-based hydrogel photocatalysis platforms. The insertion of Cu-MOF into an alginate substrate can not only turn MOF particles into macroscopic-size special-shaped structures for practical applications, but also promote the photogenerated electron-hole pairs transfer and separation for good photoelectric performances. More importantly, Cu-MOF-alginate composites can also achieve high pollutant removal by means of the synergy effect of the inherent adsorption by hydrogel and *in situ* photodegradation by Cu-MOFs. Overall, highly efficient Cu-MOF-based hydrogel photocatalysts with high light utilization efficiency, fast carrier separation, and good cycling displayed a promising application in waste-water remediation.

Through the reaction of $CuCl_2$ and 3,9-bis(pyridin-4-yl)-2,4,8,10-tetraoxaspiro[5.5]undecane (L) in CH_3CN/H_2O in a diffusion method, Cu^{II}-MOF **1** was obtained. Single-crystal X-ray diffraction (SC-XRD) analysis revealed that two-dimensional (2D) **1** consists of Cu_2Cl_4 binuclear cluster and L (Fig. 1a and Fig. S3 in Supporting information). **1** crystallizes in the monoclinic space group *P*21/*c*, and each *penta*-coordinated Cu^{2+} adopts a slightly distorted square-pyramidal geometry with $\tau = 0.11$ [33], bearing three Cl^- and two N atoms from two L. Interestingly, when **1** was immersed into a 1 mol/L CH_3CN/H_2O solution of NaI for 12 h, blood-red block crystals **2** were obtained. One-dimensional (1D) Cu^I-MOF **2** crystallizes in the monoclinic space group *C*2/*m*, and each Cu^I has a tetrahedral environment ($\tau_4 = 1.01$) [33] with two I^- and two N in a coordination shell. The rhombohedral Cu_2I_2 clusters are linked by L to form the 1D chains (Fig. S4 in Supporting information).

Comprehensive characterizations were executed to confirm the successful conversion from **1** to **2**. For example, the UV–vis spectrum of **1** displayed adsorption bands in both 352–400 nm and 719–854 nm regions, which is assigned to the $\pi \to \pi^*$ of L and d-d transitions of Cu^{2+}, respectively, and the obscure of any Cu^{2+} d-d transition bands in **2** was taken as the evidence for the reduction of Cu^{2+} to Cu^+ (Fig. S6 in Supporting information). Besides, the Cu K-edge X-ray absorption near-edge structure (XANES) spectrum of **1** gave a pre-edge energy at 8985 eV and featured the oxidation state of copper in **1** being +2, while the pre-edge features of **2** occurred at a energy of 8980.9 eV (Fig. 1b), indicating the existence of Cu^+ [34–36]. Moreover, X-ray photoelectron spectroscopy (XPS) curve of **1** showed that the signal at higher binding energy of 935.2 eV are assigned to Cu^{2+} species, and the main peak at binding energies of *ca.* 931 in **2** was assigned to Cu^+ species (Fig. 1c) [37]. The transformation from Cu^{2+} to Cu^+ species was further confirmed by Auger electron spectroscopy (AES) (Fig. S8 in Supporting information). Further, **2** exhibit luminescence thermochromism, also characteristic of Cu^I species [38]. After heating at 150 °C, non-luminescent **2** can transform to yellow-luminescent **2′** (Fig. S9 in Supporting information). SC-XRD revealed that **2′** shows structural similarity to **2**. Direct evidence has been observed that a decreased Cu⋯Cu distance is responsible for luminescent thermochromism of **2**. The shrinking of Cu⋯Cu distance leads to a decrease of Cu-I-Cu angles and Cu-I bonds length in **2′**. The emission bands of **2′** could be assigned to a combination of LMCT and d-s transitions due to Cu⋯Cu interaction within Cu_2I_2 clusters (Fig. S10 in Supporting information) [39].

Furthermore, this transformation process was monitored by electron paramagnetic resonance (EPR) and UV–vis spectroscopy. Immersion of **1** into CH_3CN/H_2O solution of NaI led to the decrease of EPR signal, in agreement with the formation of Cu^+ as **2** (silent in perpendicular mode EPR, Fig. 1d). Besides, this oxidation process was also detected by UV–vis spectroscopy at intervals based on the maximum adsorption peak of I_3^- at 352 nm [40]. As depicted in Fig. 1e, the solution of **1** slowly changed from colorless to light yellow/brown, implying the formation of I_3^-. Also, Raman spectrum (bands at 180 cm^{-1}, Fig. S11 in Supporting information) [41] and XPS (binding energies of 631.0 and 619.7 eV, Fig. S12 in Supporting information) [42] indicated the presence of natural I_2 in **2**, providing evidence for the formation of I_2 during I^- oxidation. Thus, it is proposed that the reduction of copper or the oxidation of iodide mechanism from **1** to **2** can be represented by Eq. (1). Furthermore, the atomic force microscopy (AFM) measurement indicated that the crystal surface profile undergoes significant alteration, implying a restructuring of the crystal surface. After 10 h, the relatively homogenous and flat crystal surface of the original crystal **1** becomes rough, showing holes and clefts (Fig. S13 in Supporting information). Furthermore, from the microscope, blood-red block crystals grow from the crystal surface of **1** (Fig. S14 in Supporting information).

$$\{Cu^{II}(L)Cl_2\}\cdot CH_3CN\ (\mathbf{1})\ (s) + I^-\ (l,\ excess) \rightarrow \{Cu^{I}(L)I\}\cdot 0.5I_2\cdot CH_3CN\ (\mathbf{2})\ (s) + 2Cl^- \tag{1}$$

Moreover, the stability of **1** and **2** was assessed for practical application. PXRD revealed that **1** is stable in water for 24 h but hydrolysis in an aqueous solution with pH being 2–10 or boiling water (Fig. S15 in Supporting information). In contrast, the stability of **2** remarkably increased. After soaking **2** in boiling water for 24 h, the retention of crystallinity was observed, affirming its water-stability (Fig. S16 in Supporting information). Remarkably, **2** remained its stable even in a water solution with pH 4–10 at room temperature for at least 24 h. Moreover, without the protection of an insert atmosphere, **2** can maintain a blood-red color and their particle surfaces cannot turn green due to oxidation by air-O_2 after exposure to air for at least one year, which is unusual to other Cu^I-MOFs [43,44].

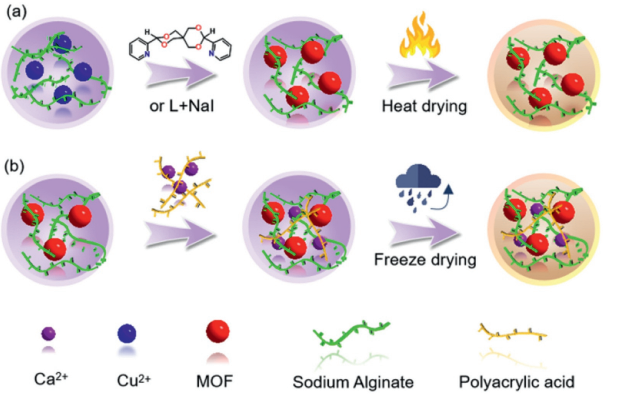

Fig. 2. The fabrication procedure of (a) **1**-Alg and (b) **2**-Alg, referred by the reported work [45].

Further, to improve the real commercial applications of MOF particles, the macroscopic-size-designable with specially ordered shapes is particularly expected [45–48]. Therefore, the Cu-MOF-alginate composite beads were tried to be fabricated. As illustrated in Fig. 2, **1**-Alg series were prepared through the *in situ* synthesis of Cu^{2+} cross-linked hydrogel and L [46]. However, immersing **1**-Alg beads into the CH_3CN/H_2O solution of NaI cannot obtain **2**-Alg beads, even though NaI can induce the transformation from **1** to **2**, which may be because that such transformation can be confined within the limited spaces of cross-linking **1**-Alg. The **2**-Alg beads were fabricated by dispersing pre-formed **2** into a sodium alginic solution, which was then immobilized into a curing solution of Ca^{2+}-polyacrylic acid.

The photo images displayed that Cu-Alg beads are transparent light-blue, yet after coordinating to L, **1**-Alg-15 beads turn into opaque light-blue, and the combination of **2** and alginate results in opaque brown (Fig. S17 in Supporting information). The morphology of Cu-MOF-alginate composites shown by scanning electron microscopy (SEM) suggested the successful loading of MOF particles (Figs. S18 and S19 in Supporting information). PXRD pattern exhibited the amorphous structure of Cu-Alg hydrogels, and the semicrystalline structures of **1**-Alg series, implying that the generation of new Cu-MOF particles distinct from **1** inside the alginate networks (Fig. S20 in Supporting information). This can be owing to the low water-stability of **1**, as well as that the preconfined coordination nature of Cu^{2+} would result in the generation of different molecular structures, and the confined alginate networks structurally hinder the construction of **1** particles [47]. By contrast, the diffraction peaks of **2**-Alg are almost the same as those of **2**, indicating that **2** is well maintained during the formation of **2**-Alg (Fig. 3a). Besides, the UV spectra of Cu-MOF-Alg beads showed similar characteristic adsorptions to their corresponding Cu-MOFs (Fig. 4a, Figs. S25 and S26 in Supporting information). Moreover, as depicted in Fig. 3b, a close insight of IR spectra revealed that for **1**-Alg series, the presence of the stronger peaks at 3447 cm^{-1} and weak peaks at 935 cm^{-1}, assigned to the *v*(-OH) and *w*(-OH), respectively, was indicative of the existence of abundant carboxyl -OH groups from alginate [45], and the shifts of Cu-N stretching at 1250 or 952 cm^{-1} compared to **1** suggested the possible existence of interactions between Cu sites and alginate [37,49]. For **2**-Alg, all characteristic peaks for **2** were obviously observed, and the existence of 1559 cm^{-1} upon the generation of beads suggested the coordination between Ca^{2+} and carboxylic groups from polyacrylic acid (Fig. 3c) [45]. The XPS spectra for Cu-MOF-Alg beads demonstrated the existence of C, O, N, I or Cl element (Fig. S21 in Supporting information), and XPS spectra of Cu $2p^3$ shown in Fig. 3d indicated the presence of Cu^+ and Cu^{2+} species for the corresponding **2**-Alg and **1**-Alg-15, which further confirmed by Auger electron spectroscopy (Fig. 3e) [37]. In the Raman spectrum of Cu-MOF-Alg beads, the band at 290–360 cm^{-1} ascribed to the vibration of Cu-Cl or Cu-I coordination bond were shifted with respect to their corresponding Cu-MOFs, indicative of the presence and changes of Cu-Cl/I bonds (Fig. S22 in Supporting information) [50]. Moreover, N_2 adsorption/desorption isotherms of Cu-MOFs and Cu-MOF-alginate composites at 77 K were tested (Fig. S23 in Supporting information), and the BET surface areas apparently increased for **1** after immobilization (Table S3 in Supporting information). Taken together, these characterizations of Cu-MOF-Alg beads suggested the successful synthesis of Cu-MOFs within the cross-linked alginate network. Furthermore, TGA analysis revealed that the MOF loading was 42.94, 65.84, and 83.47 wt% for **1**-Alg-X ($X = 10$, 15,

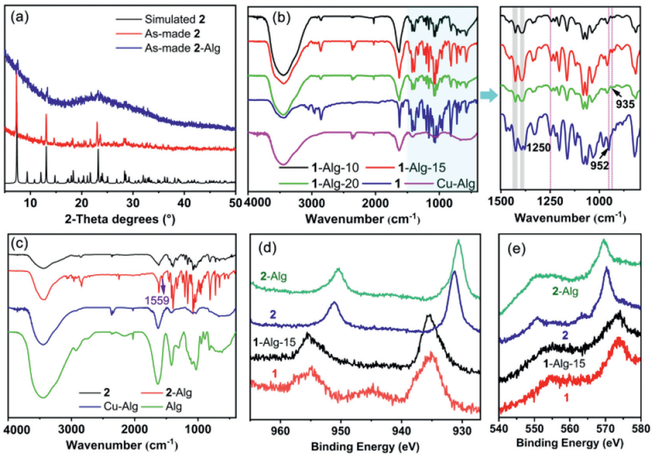

Fig. 3. (a) The PXRD pattern of **2** and **2**-Alg. (b, c) The IR spectra, (d) XPS and (e) Auger electron spectroscopy of Cu-MOFs and Cu-MOF-alginate composites.

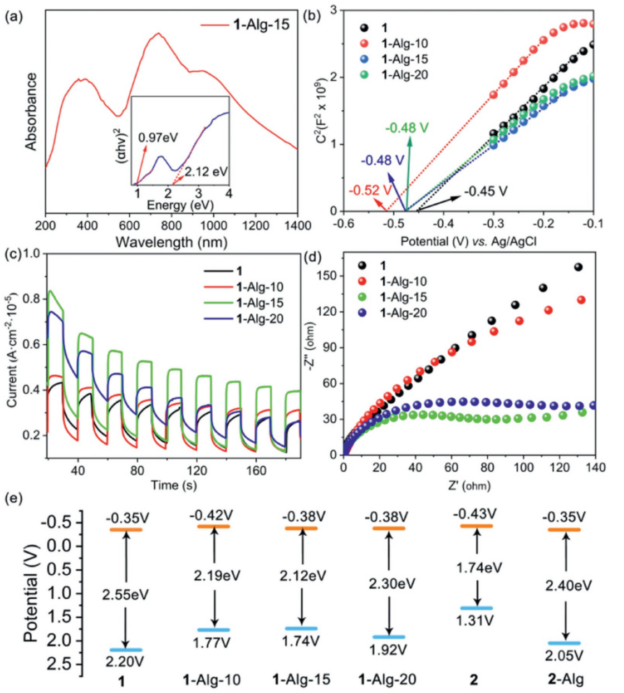

Fig. 4. (a) The UV–vis diffuse reflection spectrum of **1**-Alg-15. (b) MS curves, (c) transient photocurrent responses, and (d) EIS Nyquist plots for **1** and **1**-alginate composites. (e) The band structure diagram of Cu-MOFs and Cu-MOF-alginate composites.

and 20) bead composites, respectively, and 58.06 wt% for **2**-Alg (Fig. S24 in Supporting information).

To evaluate the photocatalytic performances of these materials, the optical and electrochemical properties were initially investigated. Solid-state UV–vis diffuse reflection spectra for Cu-MOFs and Cu-MOF-alginate composites were measured at room temperature. It was shown that all Cu-MOFs and Cu-MOF-alginate composites display a broad light adsorption range (Fig. 4a, Figs. S25 and S26 in Supporting information). For Cu-MOFs, the band-gap energies (E_g) determined from a *Tauc* plot are 2.55 and 1.74 eV for **1** and **2**, respectively. And for Cu-MOF-alginate composites, the E_g is 2.19 eV for **1**-Alg-10, 2.12 eV for **1**-Alg-15, 2.30 eV for **1**-Alg-20, and 2.40 eV for **2**-Alg. These showed that all Cu-MOFs and Cu-MOF-Alg beads could be considered as ideal n-type semiconductive materials [51–53]. Further, Mott-Schottky (MS) analysis was performed at a frequency of 1000 Hz to estimate the conduction band (CB). The flat-band potentials were determined to be −0.45, −0.52, −0.48, −0.48, −0.53, and −0.45 for **1**, **1**-Alg-10, **1**-Alg-15, **1**-Alg-20, **2**, and **2**-Alg, respectively (Fig. 4b and Fig. S27 in Supporting information), and they each CB is −0.35, −0.42, −0.38, −0.38, −0.43, and −0.35 V. Note that these CB are lower than that of $E(O_2/{\cdot}O_2^-)$ being −0.33 V (*vs.* NHE), indicating their potential applications in oxidizing organics [54,55]. Then, the valence band (VB) was estimated to be 2.20, 1.77, 1.74, 1.92, 1.31, and 2.05 V for **1**, **1**-Alg-10, **1**-Alg-15, **1**-Alg-20, **2** and **2**-Alg, respectively (Fig. 4e).

Further, transient photocurrent response and electrochemical impedance spectroscopy (EIS) were employed to evaluate the electron-hole pair separation capacities. Cu-MOF displayed enhanced photocurrents after immobilization with the order of **1**-Alg-15 > **1**-Alg-20 > **1**-Alg-10 > **1** and **2**-Alg > **2** under visible light irradiation, indicative of the better photoinduced electron-hole separation efficiency of Cu-MOF-alginate composites (Fig. 4c and Fig. S27 in Supporting information). Meanwhile, Cu-MOF-alginate composites possessed smaller charge transfer resistance than their respective Cu-MOF, which aligns with the result of photocurrent response (Fig. 4d and Fig. S28 in Supporting information). The enhanced photoinduced electron-hole transfer and separation efficiency for the immobilization of Cu-MOF into alginate perhaps as a result of the formation of an interface between Cu-MOF and alginate matrix [56], and it inspired us to investigate the photocatalytic properties of Cu-MOF and Cu-MOF-alginate composites as heterogeneous photocatalysts.

The photocatalytic performances for Cu-MOFs and Cu-MOF-alginate beads towards Cr(VI) removal were initially examined in an aqueous solution, which was monitored by the characteristic absorption band of Cr(VI) with 1,5-diphenylcarbazide at 541 nm. As depicted in Fig. 5a, about 37% and 9% adsorption efficiency of Cr(VI) for respective **1** and **2** were found and reached the adsorption-desorption equilibrium at 30 min. Then under Xe-light irradiation, approximately 85% and 96% removal efficiency at subsequent 25 min were observed for **1** and **2** with the pseudo-first-order reaction kinetic constants (k) being 0.06 and 0.12 min^{-1} (Figs. S30-S32 in Supporting information). After incorporating them into alginate substrate, the Cr(VI) removal obviously enhanced, and the removal efficiency followed the order of **1**-Alg-15 > **1**-Alg-20 > **1**-Alg-10 > **1** (removal efficiency X at 15 min and k: 88% and 0.07 min^{-1} for **1**-Alg-10, 96% and 0.14 min^{-1} for **1**-Alg-15, 92% and 0.11 min^{-1} for **1**-Alg-20) (Figs. S30-S32). Note that compared to Cu-MOF, Cu-MOF-Alg series exhibited apparently improved adsorption capacity of Cr(VI) upon achieving the adsorption-desorption equilibrium. Accordingly, the enhanced Cr(VI) removal capacity of Cu-MOF-alginate composites relative to Cu-MOFs is perhaps owing to the synergistic effects of Cr(VI) adsorption for hydrogel and *in situ* photocatalytic Cr(VI) reduction for Cu-MOFs. Specifically, Cr(VI) can nearly complete removal at 15 min for **1**-Alg-15 and 40 min for **1**, and 25 min for **2**-Alg and 30 min for **2**, which is superior or comparative to the reported works [57,58].

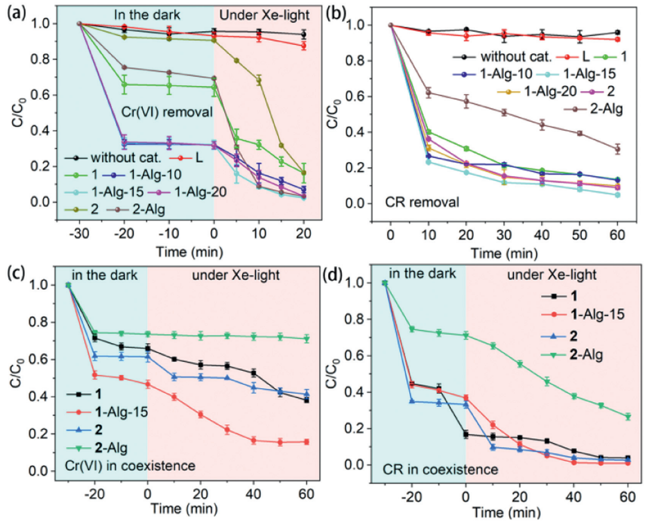

Fig. 5. The Cr(VI) and CR removal efficiency of Cu-MOFs and Cu-MOF-alginate composites in aqueous solution (a, b) without or (c, d) with the coexistence of CR and Cr(VI).

Besides, the CR decolorization was also examined to evaluate photocatalytic performances, which was monitored by the characteristic absorption band of CR at 498 nm. Control experiments showed that no obvious decay in CR concentration with L as a catalyst or without catalyst under Xe-light irradiation (Fig. 5b). Meanwhile, a comparisonfs experiment in dark conditions showed that the Cu-MOFs and Cu-MOF-alginate beads possess the adsorption capacity of CR with the order: **1**-Alg-10/15 (59%) > **1**-Alg-20 (46%) > **1** (39%), and **2** (58%) > **2**-Alg (33%) (Figs. S33-S38 in Supporting information). Under Xe-light irradiation, with time increasing, the CR removal efficiency for **1** and **2** gradually enhanced, and approximately 85% and 92% removal at 60 min were observed. However, unlike the enhanced Cr(VI) elimination of **1** and **2** after immobilization, the CR removal (70%) for **2**-Alg was worse than that of **2**, which may be due to the lower porosity of **2**-Alg compared with **2**, confirmed by N_2 adsorption test (Fig. S23). By contrast, a noticeable CR degradation was successfully achieved with the tendency of **1**-Alg-15 (95%) > **1**-Alg-20 (90%) > **1**-Alg-10 (86%) > **1** (85%) at 60 min, which is consistent with the charge separation capacity of **1** and **1**-alginate beads, indicating the enhanced photocatalytic activity towards CR decolorization upon incorporating **1** into an alginate substrate.

Inspired by the above results, the simultaneous removal CR and Cr(VI) experiment was conducted and monitored by the characteristic absorption band of Cr(VI) and CR at 354 and 491 nm, respectively (Figs. S39-S42 in Supporting information). As shown in Figs. 5c and d, only approximately 44% and 50% removal efficiency of Cr(VI) at 30 min, while 96% and 97% decolorization of CR at 60 min can be observed for **1** and **2**, respectively. Compared to the isolated CR or Cr(VI) removal, both Cu-MOFs displayed an enhanced decontamination of CR yet decreased reduction of Cr(VI) upon CR and Cr(VI) in coexistence. For Cu-MOF-alginate composites, about 78% and 28% Cr(VI) removal efficiency at 30 min, and 99% and 74% CR decolorization at 60 min were found for respective **1**-Alg-15 and **2**-Alg. It can be found that **1**-Alg-15 displays superior decontamination of Cr(VI) and CR with respect to **1** under the coexistence of CR and Cr(VI), while **2**-Alg are worse than that of **2**. The existence of Cr(VI) performs a positive effect on the decontamination of CR for all Cu-MOF-alginate composites, yet the CR resulted in the reduced removal of Cr(VI). Thus, both Cu-MOFs or

Cu-MOF-alginate composites showcased an admirable promotion of CR decolorization *via* the existence of Cr(VI). Above all, **1**-Alg-15 presented an excellent photocatalytic performance towards the simultaneous removal of Cr(VI) and CR, quite comparative or superior to the reported photocatalysts (Table S4 in Supporting information).

Moreover, the Cr(VI) or CR removal capacity for Cu-MOFs and Cu-MOF-alginate composites in Feng-river was also investigated (Figs. S43-S49 in Supporting information). For Cr(VI), approximately 93%, 94%, 99%, 97%, 97%, and 97% removal were observed using **1**, **1**-Alg-10, **1**-Alg-15, **1**-Alg-20, **2**, **2**-Alg at 30 min, respectively, and nearly complete Cr(VI) removal at 15 min for **1**-Alg-15 and 20 min for **2**-Alg. And for CR, both Cu-MOFs and **1**-Alg beads were observed to display excellent CR decolorization performance, and the best behaviors can be found by using **1**-Alg-15 and **1**-Alg-20 composites as photocatalysts, in which nearly complete CR decolorization was observed at a short time of 20 min.

Moreover, the cyclability and stability of both Cu-MOFs and Cu-MOF-alginate composites towards Cr(VI) or/and CR removal were investigated (Figs. S50-S60 in Supporting information). Compared to **1**, **2** displayed increased recyclability and stability without obvious structure change after three cycles. Of particular interest, even though the stability became worse, the cyclability of pollutants removal greatly enhanced upon Cu-MOFs were treated into Cu-MOF-alginate composites. Specifically, after eleven test cycles, the Cr(VI) removal efficiency can be maintained at up to 96% for **1**-Alg-15, and a high cyclability for **2**-Alg was also found to be 95% after fourteen runs. Moreover, over 90% removal efficiency of CR for **1**-Alg-15 has been observed after ten consecutive runs. These results positively point out that the transformation from **1** to **2** can efficiently improve the Cr(VI)/CR removal efficiency, recyclability and stability, as well as **1**-alginate composite displayed high photocatalytic activity and could be deemed potentially usable in real river water.

Given the excellent photocatalytic performance of **1**-Alg-15, the mechanism of CR and Cr(VI) decontamination over **1**-Alg-15 was speculated. Initially, a series of trapping experiments and *in situ* ERP tests were executed. Specifically, the addition of *p*-benzoquinone ($^{\cdot}O_2^-$ scavenger) caused the obviously decreased removal efficiency of CR, indicating that $^{\cdot}O_2^-$ is the key participant in the photodegradation of CR over **1**-Alg-15 (Table S6 in Supporting information). Additionally, the EPR experiments also corroborated the presence of $^{\cdot}O_2^-$ by employing the trapping agent of 5,5-dimethyl-pyrroline-*N*-oxide (DMPO) (Fig. S61 in Supporting information). By contrast, no photocatalytic suppression was observed upon the addition of propane-2-ol ($^{\cdot}OH$ scavenger), demonstrating that $^{\cdot}OH$ is not the ROS in this reaction. Furthermore, the reduced CR decontamination efficiency was found by adding $AgNO_3$ (electron scavenger) or KI (hole scavenger), revealing the production of photogenerated electrons and holes. And the decreased Cr(VI) removal efficiency by introducing the $AgNO_3$ showed the participation of e^- in the reduction reaction (Table S7 in Supporting information).

In view of the abovementioned analysis and reported literature [59], a plausible photodegradation mechanism of CR and Cr(VI) over **1**-Alg-15 was provided (Fig. S62 in Supporting information). Under the visible-light irradiation, Cu-MOF embedded in the alginate network was excited to form the photogenerative electron and holes, in which the electron on the CB, on the one hand reduced the Cr(VI) into Cr(III), and on the other hand reacted with the air-O_2 into $^{\cdot}O_2^-$, which further oxidize CR into CO_2 and H_2O. Additionally, the holes accumulated on the VB can also oxidize and mineralize CR pollutants. Note that the alginate can act as a transmitter for $^{\cdot}O_2^-$, electron and hole to further improve the photodegradation performances.

In summary, we offered a general structuring strategy by the integration of Cu-MOF and alginate substrate into visible-light driven Cu-MOF-based hydrogel photocatalysts bearing excellent performance in the removal of CR and Cr(VI). On the one hand, the incorporation of Cu-MOF into hydrogel can efficiently promote the photogenerated carrier transfer and separation for improving photocatalytic degradation pollutants. On the other hand, the macroscopic-size sphere-shaped photocatalysts can be easily separated and recovered for practical applications. Furthermore, the photodegradation mechanism showed the photocatalytic performance of Cu-MOF-alginate composite is associated with $^{\cdot}O_2^-$, e^- and h^+, and hydrogel played a significant role in storing and shuttling electrons, as well as good adsorption. Accordingly, Cu-MOF-alginate composite beads can be recommended as efficient photocatalysts in terms of high photocatalytic performance, environmental sustainability, facile separation, and good cycling toward the removal of CR and Cr(VI) from the wastewater.

Declaration of competing interest

The authors declare that they have no known competing financial interests or personal relationships that could have appeared to influence the work reported in this paper.

CRediT authorship contribution statement

Quanquan Li: Conceptualization, Investigation, Validation, Visualization, Writing – original draft, Formal analysis, Data curation. **Chenzhu Zhao:** Data curation, Investigation, Validation. **Shanshan Jia:** Data curation, Formal analysis, Validation. **Qiang Chen:** Data curation, Formal analysis, Validation. **Xusheng Li:** Data curation, Investigation, Validation. **Mengyao She:** Data curation, Funding acquisition, Investigation, Validation. **Hua Liu:** Conceptualization, Investigation, Validation, Visualization, Writing – review & editing. **Ping Liu:** Conceptualization, Funding acquisition, Project administration, Supervision, Validation, Writing – review & editing. **Yaoyu Wang:** Conceptualization, Supervision, Validation. **Jianli Li:** Conceptualization, Funding acquisition, Project administration, Supervision, Validation, Writing – review & editing.

Acknowledgments

This work was financially supported by the National Natural Science Foundation of China (Nos. 22077099, 22171223 and 22307102), the Innovation Capability Support Program of Shaanxi (Nos. 2023-CX-TD-75 and 2022KJXX-32), the Technology Innovation Leading Program of Shaanxi (Nos. 2023KXJ-209 and 2024QCY-KXJ-142), the Natural Science Basic Research Program of Shaanxi (Nos. 2023-JC-YB-141 and 2022JQ-151), the Key Research and Development Program of Shaanxi (No. 2024GH-ZDXM-22), Young Talent Fund of Association for Science and Technology in Shaanxi, China (No. SWYY202206), the Shaanxi Fundamental Science Research Project for Chemistry & Biology (Nos. 22JHZ010 and 22JHQ080), the Yan'an City Science and Technology Project (No. 2022SLZDCY-002).

Supplementary materials

Supplementary material associated with this article can be found, in the online version, at doi:10.1016/j.cclet.2024.109936.

References

[1] S. Rojas, P. Horcajada, Chem. Rev. 120 (2020) 8378–8415.
[2] K. Wu, X.Y. Liu, P.W. Cheng, et al., J. Am. Chem. Soc. 145 (2023) 18931–18938.

[3] T.H. Wang, Z. Zhao, S. Garcia-Segura, et al., Appl. Catal. B: Environ. 342 (2024) 123397.
[4] Y.T. Wang, Y. Qin, X.L. Zhao, et al., Chin. Chem. Lett. 34 (2023) 107576.
[5] M. Mon, R. Bruno, E. Tiburcio, et al., J. Am. Chem. Soc. 141 (2019) 13601–13609.
[6] B.M. Jun, S.S. Elanchezhiyan, Y. Yoon, et al., Chem. Eng. J. 393 (2020) 124733.
[7] D. Kandi, S. Martha, A. Thirumurugan, K.M. Parida, ACS Omega 2 (2017) 9040–9056.
[8] S. Lotfi, K. Fischer, A. Schulze, A.I. Schäfer, Nat. Nanotechnol. 17 (2022) 417–423.
[9] S. Ren, J. Dong, X. Duan, et al., Chem. Eng. J. 460 (2023) 141884.
[10] J. Meng, Y. Zhou, D. Li, X. Jiang, Sci. Bull. 68 (2023) 1522–1530.
[11] X. Chen, H. Ma, X. Ji, et al., Water. Res. 243 (2023) 120314.
[12] J. Wang, Y. Mao, R. Zhang, et al., Adv. Sci. 9 (2022) 2204036.
[13] Z. Guo, Z. Ren, H. Gao, et al., Appl. Surf. Sci. 644 (2024) 158732.
[14] Y. Hu, Z. Zhong, M. Lu, et al., Chem. Eng. J. 450 (2022) 137964.
[15] J. Xiao, Y. Xie, J. Rabeah, et al., Acc. Chem. Res. 53 (2020) 1024–1033.
[16] H. Fu, Y. Deng, Z. Cai, et al., J. Hazard. Mater. 463 (2024) 132820.
[17] X. Bai, Y. Du, X. Hu, et al., Appl. Catal. B: Environ. 239 (2018) 204–213.
[18] A. Chen, Z. Bian, J. Xu, et al., Chemosphere 188 (2017) 659–666.
[19] X. Bai, J. Wan, J. Jia, et al., Mater. Lett. 222 (2018) 187–191.
[20] W. Lei, N. Suzuki, C. Terashima, A. Fujishima, Front. Energy 15 (2021) 577–595.
[21] W. Lei, S. Qi, Q. Rong, et al., Adv. Mater. 31 (2019) 1808217.
[22] W. Jiang, Y. Liu, J. Wang, et al., Adv. Mater. Interfaces 3 (2016) 1500502.
[23] X. Chen, Q. Chen, W. Jiang, et al., Appl. Catal. B: Environ. 211 (2017) 106–113.
[24] H. Zhu, Z. Li, J. Yang, Chem. Eng. J. 334 (2018) 1679–1690.
[25] T. Luo, L. Gilmanova, S. Kaskel, Coord. Chem. Rev. 490 (2023) 215210.
[26] Y. Hao, E.K. Papazyan, Y. Ba, Y. Liu, ACS Catal. 12 (2021) 363–371.
[27] X. Liu, B. Liu, G. Li, Y. Liu, J. Mater. Chem. A 6 (2018) 17177–17185.
[28] Y. Wu, X. Wang, K.O. Kirlikovali, et al., Angew. Chem. Int. Ed. 61 (2022) e202117528.
[29] W.F. Hu, S. Chen, H.C. Hao, H. Jiang, AIChe J. 68 (2022) e17879.
[30] L.J. Chen, S.J. Chen, Y. Qin, et al., J. Am. Chem. Soc. 140 (2018) 5049–5052.
[31] P.P. Jia, Y.X. Hu, Z.Y. Zeng, et al., Chin. Chem. Lett. 34 (2023) 107511.
[32] H.Y. Lin, L.Y. Zhou, F. Mei, et al., Angew. Chem. Int. Ed. 62 (2023) e202301900.
[33] A.W. Addison, T.N. Rao, J. Reedijk, et al., J. Chem. Soc. Dalton Trans. 7 (1984) 1349–1356.
[34] C. He, G. Zhang, J. Ke, et al., J. Am. Chem. Soc. 135 (2013) 488–493.
[35] G. Zhang, H. Yi, G. Zhang, et al., J. Am. Chem. Soc. 136 (2014) 924–926.
[36] H. Yi, D. Yang, Y. Luo, et al., Organometallics 35 (2016) 1426–1429.
[37] Y. Zhang, Q. Zhou, Z.F. Qiu, et al., Adv. Funct. Mater. 32 (2022) 2203677.
[38] Y. Zhang, M. Schulz, M. Wächtler, et al., Coord. Chem. Rev. 356 (2018) 127–146.
[39] T.H. Kim, Y.W. Shin, J.H. Jung, et al., Angew. Chem. Int. Ed. 47 (2008) 685–688.
[40] H.H. Lee, I.H. Park, S. Kim, et al., Chem. Sci. 8 (2017) 2592–2596.
[41] T.J. Matemb Ma Ntep, H. Reinsch, C. Schlüsener, et al., Inorg. Chem. 58 (2019) 10965–10973.
[42] Z. Yan, Y. Yuan, Y. Tian, et al., Angew. Chem. Int. Ed. 54 (2015) 12733–12737.
[43] J.P. Zhang, S. Kitagawa, J. Am. Chem. Soc. 130 (2008) 907–917.
[44] S.Y. Liu, X.L. Qi, R.B. Lin, et al., Adv. Funct. Mater. 24 (2014) 5866–5872.
[45] S. Yang, L. Peng, O.A. Syzgantseva, et al., J. Am. Chem. Soc. 142 (2020) 13415–13425.
[46] H. Zhu, Q. Zhang, S. Zhu, A.C.S. Appl, Mater. Inter. 8 (2016) 17395–17401.
[47] S.J. Lee, T. Hann, S.H. Park, ACS Appl. Mater. Inter. 12 (2020) 16319–16326.
[48] M. Li, W. Huang, B. Tang, et al., Ind. Eng. Chem. Res. 59 (2020) 18835–18843.
[49] X. Xie, X. Zhang, M. Xie, et al., Nat. Commun. 13 (2022) 63.
[50] A. Sabatini, L. Sacconi, J. Am. Chem. Soc. 86 (1964) 17–20.
[51] H. Liu, Q. Li, P. Pan, et al., Chin. Chem. Lett. 34 (2023) 108562.
[52] T. Luo, L. Li, Y. Chen, et al., Nat. Commun. 12 (2021) 3583.
[53] S.Q. Wang, X. Gu, X. Wang, et al., Chem. Eng. J. 429 (2022) 132157.
[54] H. Liu, Q.Q. Li, L. Zhou, et al., J. Am. Chem. Soc. 145 (2023) 17588–17596.
[55] Q.Q. Li, P.H. Pan, H. Liu, et al., Inorg. Chem. 62 (2023) 17182–17190.
[56] G. Lu, H. Tang, Y. Huan, et al., Adv. Funct. Mater. 20 (2010) 1714–1720.
[57] D.Y. Peng, H.Y. Zeng, J. Xiong, et al., J. Alloys Compd. 912 (2022) 165063.
[58] X. Li, E. Almatrafi, H. Wang, et al., Chem. Eng. J. 457 (2023) 141087.
[59] B. Li, X. Zhao, Y. Huang, et al., Environ. Sci. Pollut. R 30 (2023) 122537.